Intermetallics 175 (2024) 108469

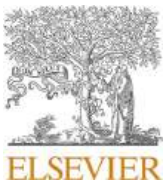

Contents lists available at ScienceDirect

Intermetallics

journal homepage: www.elsevier.com/locate/intermet

Machine learning assisted design of new ductile high-entropy alloys: Application to Al-Cr-Nb-Ti-V-Zr system

Denis Klimenko [a,*], Nikita Stepanov [a,b], Roman Ryltsev [c], Nikita Yurchenko [a,b], Sergey Zherebtsov [a,b]

[a] Laboratory of Bulk Nanostructured Materials, Belgorod State University, Belgorod, 308015, Russia
[b] World-Class Research Center "Advanced Digital Technologies", State Marine Technical University, Saint Petersburg, 198095, Russia
[c] Institute of Metallurgy of the Ural Branch of the Russian Academy of Sciences, Ekaterinburg, 620016, Russia

ARTICLE INFO

Keywords:
High-entropy alloys
Refractory high-entropy alloys
Machine learning
Data-driven machine learning models
Plasticity

ABSTRACT

The search for new high-entropy alloys (HEAs) with desired properties is an urgent problem that is hardly solvable experimentally due to the extremely large number of possible alloy compositions. Thus, methods for theoretical prediction of HEA's properties play a key role. Currently, effective predictive models are based on machine learning methods and modern data analysis algorithms. Here we address developing data-driven machine learning models (DDML) to predict the ductility of HEAs. We have built several DDMLs and found that the best approach is based on the Support Vector Classifier, which significantly outperforms phenomenological models (balanced accuracy of 0.784 and F-score of 0.824). By combining this model with a previously developed yield strength prediction model, we have predicted and fabricated novel HEAs of the Al-Cr-Nb-Ti-V-Zr system with good mechanical properties. An obtained $Al_1Cr_9Nb_{35}Ti_5V_{40}Zr_{10}$ alloy demonstrates a combination of high strength at room and elevated temperature, combined with good ductility at room temperature.

1. Introduction

In the thousands of years, alloys were produced by addition of property-enhancing minor elements into one or two principal elements. Examples of as-fabricated materials are the most widely used alloys, such as steel, bronzes, aluminum alloys, titanium alloys, TiAl intermetallic alloys, etc. Traditionally, it was believed that an increase in the proportion of the minor elements would lead to the formation of many intermetallic phases, some of which could lead to a deterioration in the mechanical and functional properties of alloys.

However, Yeh et al. [1] and Cantor et al. [2] in 2004 showed that alloys with five or more elements in equatomic concentration can have a single-phase random solid solution. It was proposed that an increase in the contribution of configurational entropy for such alloys leads to stabilization of the single-phase solid solution, therefore such alloys were called high-entropy alloys (HEAs). Further research has shown that this contribution is not so significant [3–5], so these alloys are also named as multicomponent alloys, multi-principal-element alloys, compositionally-complex alloys, or complex concentrated alloys [6]. This new paradigm for fabricating alloys concentrated in the central unknown space of chemical composition diagrams, rather than at the corners of this space, provides the presence of an enormous number of new alloys. Numerous papers devoted to HEAs (including reviews [3, 7–11]) reveal great interest to their discover in the scientific community.

Many HEAs were found to be attractive due to their high strength (including high-temperature strength), structural stability, hardness, wear resistance, as well as good corrosion and oxidation resistance [1, 12–17]. All that allows considering HEAs as promising materials for various fields. A relevant example is HEAs based on refractory metals (RHEA), which are promising candidates for high-temperature applications. Among RHEAs, the NbMoTaW and VNbMoTaW alloys reveal superb strength at 1600 °C. However, the high density ($\rho > 12$ g/cm^3) of these alloys significantly limits their usability [18,19]. The use of lighter refractory elements makes it possible to reduce the density of the alloys (as well as the range of operating temperatures). For example, the HfNbTaTiZr alloy ($\rho \sim 9.9$ g/cm^3) shows the yield strength of $\sigma_y = 92$ MPa at 1200 °C [20]. The introduction of chromium into the $CrMo_{0.5}NbTa_{0.5}TiZr$ alloy reduces density down to $\rho \sim 8.2$ g/cm^3 keeping the high yield strength at 1200 °C ($\sigma_y = 171$ MPa) [21]. Due to presence of aluminum, the $AlMo_{0.5}NbTaTiZr$ alloy has low density ($\rho \sim$

* Corresponding author.
E-mail address: klimenko@bsu.edu.ru (D. Klimenko).

https://doi.org/10.1016/j.intermet.2024.108469
Received 1 July 2024; Received in revised form 14 August 2024; Accepted 31 August 2024
Available online 9 September 2024

7.4 g/cm^3) with high yield strength $\sigma_y = 250$ MPa at 1200 °C [22]. The decrease in fraction of heavy refractory metals can further reduce the density of the alloys, but at the same time decreases potential operating temperatures. However, alloys of the (Al)-Cr-Nb-Ti-V-Zr system with a specific yield strength at temperatures of 800–1000 °C superior to modern nickel alloys were already developed [23,24].

However, in an effort to improve strength characteristics, we often obtain alloys with low ductility (especially at room temperature). This is especially true for RHEAs, since their main phase is usually the BCC phase, which has less plasticity compared to FCC. For example, among the above-mentioned RHEAs, most have deformation before failure of less than 5 %. The actual practical use of such alloys as structural materials is difficult because limited plasticity complicates their deformation and mechanical processing.

A large number of principal elements opens a huge potential for the material design. On the other hand, the traditional trial-and-error method to search for new alloys is too labor-intensive and unpromising for the vast composition space of HEAs. Thus, methods for theoretical prediction of structure and properties of HEAs play a key role.

The most straightforward methods for theoretical investigation of metallic alloys are based on atomistic simulations, where one calculates properties by averaging over microscopic trajectories. The central object of such simulations is the potential energy surface (PES) whose derivatives are interatomic forces. The estimation of PES in HEAs is an extremely complicated problem. Indeed, with an increase in the number of principal elements, the number of pairs of interactions of different atomic types increases significantly. Besides the interactions of a higher order is hardly possible due to the exponential growth of the possible interactions. This leads to the fact that simple model functions widely used in atomic simulations for approximating PES (for example, the embedded atom method (EAM)) often provide low accuracy for HEAs. Moreover, parametrization of such potentials for multicomponent alloys requires extensive training databases and robust, efficient, and, preferably, fully automated fitting strategies, whose implementation is usually far from straightforward [25–27]. Nevertheless, such approaches can be used to predict the plasticity of HEAs. Daramola et al. [28] constructed the EAM potential for the CrFeMnNi system and calculated some characteristics of the equiatomic alloy CrFeMnNi - the stability of the FCC phase, elastic constants, and stacking fault energy. Based on this data the dynamics a ½⟨110⟩{111} edge dislocation in the equiatomic CrFeMnNi alloy in the temperature range 0–900 K were simulated by molecular dynamics. Such approaches can demonstrate good accuracy, but require significant computational effort for each individual alloy and are poorly suited for screening vast compositional spaces.

In the case of first-principles simulations, the PES is calculated directly by solving the Schrödinger equation for electrons (foremost using density functional theory (DFT) approximations). Such *ab initio* methods provide high accuracy and predictive ability but have a high computational cost. First-principles simulations of HEAs consisting of more than 5 principal elements and non-stoichiometric compositions require the use of large model supercells (up to more than 1000 atoms) to cover such effects as various degrees of randomness and order distribution of these elements [29–32], extended dislocation core structures [33,34], etc. That makes *ab initio* simulations of HEAs extremely computationally expensive [35]. However, *ab initio* methods can also be used to predict the plasticity of RHEAs. Gao et al. [36] used three different *ab initio* methods to predict NbMoTaTiV plasticity at room temperature. Good agreement with experimental data was obtained, but such approaches are also poorly suited for screening large compositional spaces.

Analytical empirical models allow calculating some properties of HEAs with high accuracy, but they usually have a limited scope of applicability or require either specific data or tunable parameters. A typical example is the solid solution strengthening model for calculating the yield strength. A few such models adopted for HEAs show good agreement with theoretical and experimental data, but they are applicable for only single-phase alloys [37–40]. An example of using this approach to predict plasticity is the crystal plasticity with finite element method (CPFEM). CPFEM are based on the constitutive model of single crystal. In early studies, experimental data are used to back-fit the constitutive model of single crystal [41]. While microscopic material coefficients in physical mechanism are combined to solve the constitutive model in order to connect more closely macroscopic performance and microscopic mechanism [42–46]. As with previous approaches, such models are characterized by high computational complexity, resource consumption and time consumption.

Phenomenological rules based on experimental data are another possible way for predicting different characteristics of HEAs, such as single-phase or multiphase composition [47–54], the presence of certain phase [55–58] or plasticity[59–61]. The general problems of this approach are low-accuracy, unbalanced score and thus limited applicability [62,63]. The phenomenological rules of ductility based on Pettifor and Pugh criteria (G/B) [64], Valence Electron Concentration (VEC) criterion [65] or Rice and Thomson criterion Gb/γ [9] can be used to predict plasticity. However, such models are designed for single-phase alloys and also have low accuracy [62].

The last decade has been marked by the revolutionary development of artificial intelligence and machine learning (ML) [66]. This revolution has not only fundamentally changed several domains of computer science (such as computer vision and natural language processing) but has also significantly affected culture, technology, and science (including materials science). ML models are generally flexible and complicated functions that can be parametrized (trained) on experimental and/or computation data to solve successfully different problems, such as classification and regression. Thus, ML is a promising tool to address the aforementioned challenges in the theoretical modeling of HEAs. For example, the use of ML models like neural networks as effective regressors for PES makes it possible to achieve nearly *ab initio* accuracy in atomistic simulations of HEAs with orders of magnitude less computational costs [67]. This allows researchers to perform accurate first-principles simulations of materials with more than millions of atoms [68]. However, the use of machine learning potentials for exploratory research of the properties of structural materials is hardly possible. Indeed, direct atomistic simulations of such properties as yield strength for dozens of alloys are so computationally expensive that they become almost unrealizable. However, for exampleб combining CPFEM with artificial neural networks [69] this reduces the cost of resources and time, although such models are still limited in their suitability for screening large compositional spaces.

Fortunately, there is another way, called data mining or data-driven approach, which involves making predictions by summarizing the available literature data and searching for hidden relations in these data using machine learning algorithms. A large amount of various data about HEAs collected from experiments or computations allow performing ML-based predictions of their properties [70,71]. For example, data-driven ML models for predicting the phase composition of HEAs are widely used. The models are distinguished by their accuracy and range of predicted phase composition, from classifying alloys into single-phase and multiphase [72–76] to predicting the composition of a whole range of phases [77–81], including a different type of intermetallic phases [82]. Also, data-driven ML models allow predicting mechanical properties such as elastic moduli, microhardness, and yield strength at both room and elevated temperatures [83–86]. Nevertheless, using the example of Mg alloys, the possibility of predicting plasticity using such models was shown [87]. However, little attention has been paid to predict the ductility of RHEAs using data-driven ML [88].

Such models allow achieving high accuracy, low computational complexity and high calculation speed. That is, they are best suited for screening large compositional spaces, which is extremely important for searching new RHEAs. In this work, we used the DDML model combined with an elastic net to select training features to predict the plasticity of RHEAs at room temperature. The model was used to produce new

Table 1
Descriptors and equations for their calculations. The general formulas for $\overline{X}$ and δX are presented in the common third column for the corresponding rows.

Description	Abbreviation	Formula
Mixing Enthalpy	ΔS_{mix}	$\Delta S_{mix} = -R\sum c_i \ln c_i$
Mixing Entropy	ΔH_{mix}	$\Delta H_{mix} = \sum\sum 4\Delta H_{ij}^{mix} c_i c_j$
Combining effect of Mixing Enthalpy and Mixing Entropy	Ω	$\Omega = \frac{T_m \Delta S_{mix}}{\lvert\Delta H_{mix}\rvert} \quad T_m = \sum c_i T_i$
Atomic size mismatch	R	$\overline{R} = \sum c_i R_i$
		$\delta R = \sqrt{\sum c_i \left(1 - R_i/\overline{R}\right)^2}$
	Λ	$\Lambda = \Delta S_{mix}/\delta R^2$
	γ	$\gamma = \left(1 - \sqrt{\frac{(R_s+\overline{R})^2 - \overline{R}^2}{(R_s+\overline{R})^2}}\right) / \left(1 - \sqrt{\frac{(R_l+\overline{R})^2 - \overline{R}^2}{(R_l+\overline{R})^2}}\right)$
Pauling electronegativity	χ_P	$\overline{X} = \sum c_i X_i$
Allen electronegativity	χ_A	
Martynov-Batsanov electronegativity	χ_{MB}	$\delta X = \sqrt{\sum c_i \left(1 - X_i/\overline{X}\right)^2}$
Alfred-Rochow electronegativity	χ_{AR}	
Absolute electronegativity	χ_{Abs}	
Valence electron concentration	VEC	
Melting point	MT	
Cohesive energy of solid	CE	
Compression Modulus	MC	
First ionization energy	FIE	
Second ionization energy	SIE	
Third ionization energy	TIE	
Work function	WF	
Atomic number	AN	
Quantum number	QN	
Column in periodic table	C	
Relative atomic mass	RAM	
Atom volume	VA	
Atomic environment number	AEN	
Miedema chemical potential	CPM	
Slater effective nuclear charge	NCE	
Clementi effective charge nuclear	CNE	
Boiling temperature	TB	
Vaporization enthalpy	EV	
Melting enthalpy	EM	
Atomization enthalpy	EA	
Yagoda ionic radii	RI	
Covalent radii	RC	
Schubert valence electron distance	DVE	
Schubert core electron distance	DCE	
Density	D	

ductile alloys for the Al-Cr-Nb-Ti-V-Zr system.

2. materials and methods

2.1. Data collection and feature selection

A dataset for this article was constructed on the basis of experimental data reported in peer-reviewed research articles. The dataset was mainly formed using compressed fracture strain because its values are more widely presented in the literature. If data on elongation at break were available from several sources, the average value was included in the dataset. The alloys in the dataset were classified as "ductile" and "non-ductile" with a threshold value of 10 %. The dataset was supplemented by tensile fracture strain for alloys with superb (elongation to fracture >50 %) and poor (elongation to fracture <5 %) plasticity. These alloys have been classified as "ductile" and "non-ductile", respectively. In summary, the dataset included 221 entries, of which 57 were "non-ductile" and 164 were "ductile".

A crucial step in developing a ML model is the choice of input features (descriptors) that determine the value of predicting properties or belonging to a certain class. Different approaches can be used to select training features. One of the most widely used and effective approaches for feature selection is based on the correlation value between a feature and a target parameter [89]. The effective set of features can also be found by iterating over an array of possible sets of features using evolution algorithms [76]. A possible option is to select the set of features that are associated with the target parameter within existing models or hypotheses [90]. In our work, the elastic net, which is the linear mixture of ridge (L_2 norm) and LASSO (L_1 norm) regularization terms, was used for feature selection with L_1 ratio of 0.5. The coefficients of elastic net regression represent the linear relationship between the features and the target variable, adjusted by the regularization terms. The greater the absolute value of the coefficient, the stronger the effect of the corresponding feature on the target variable. The sign of the coefficient indicates the direction of the effect: positive for positive correlation, negative for negative correlation. The coefficients that are zero indicate that the corresponding features are not relevant for the model, and they are eliminated by the LASSO penalty. Therefore, one can use the coefficients of elastic net regression to rank the features by their importance and select the ones that have non-zero coefficients.

In the first step, for each entry in the dataset, 69 descriptors were calculated [76]. Most of them were molar average values $\overline{X}$ and mismatch values δX of different physicochemical characteristics. (Table 1). Descriptors were normalized via Eq.(1) to make their values comparable:

$$X_i^{norm} = \frac{X_i - X_i^{min}}{X_i^{max} - X_i^{min}} \tag{1}$$

where X_i^{min} and X_i^{max} are the maximum and minimum values of X_i features, respectively.

The elastic net was used in two variants, as a regression model (for prediction of fracture strain of alloys) and as classifier model (for classification of alloys as "ductile" and "non-ductile").

The selection of features was performed by next steps for both variant of the elastic set:

1) *Separation of validation dataset.* For checking elastic set and another model of machine, learning validation dataset was selected. 5 entries of both classes (10 entries total) were randomly chosen. The validation set was not used in training of machine learning model (elastic set and another model on next stage), only for checking models and calculations the accuracy metrics.
2) *Dataset sampling.* Due to severe skew in the class distribution of our dataset random undersampling was used for dataset sampling.
3) *Elastic net.* The coefficients for each feature were calculated.
4) *Normalization of coefficients.* Coefficients with maximum modulus was selected and then all the coefficients were normalized to the maximum values while maintaining their sign.

This sequence of calculations was performed 10 times to reduce the effect of random splitting and averaged. After that, the features were ranked by their importance based on the modulus of the normalized coefficient (Fig.S1, Fig.S2 and Table S1). Ones bigger than the threshold value were included in the set of features for training machine-learning models.

Since the coefficient values change continuously from 0 to 1, choosing the features cutoff threshold is a difficult task. As part of this work, the features cutoff value varied from 0.05 to 1 with a step of 0.05.

All features whose coefficient is equal to or greater than the feature cutoff threshold were included in the set of features for training models. Based on each set of features, after applying various balancing techniques, datasets were generated for training models.

As noted above, our dataset shows a strong disproportion towards "ductile" alloys. Serious data imbalances can influence on the accuracy of the machine learning models. One possible method to eliminate the influence of imbalance is to balance the dataset (each output class is represented by the same number of entries). We used both undersampling by random undersampling and oversampling by Adaptive Synthetic (ADASYN) and Synthetic Minority Over-sampling Technique (SMOTE) algorithms. For each balancing technique, 10 datasets were formed. All of these datasets were used for training machine-learning models and averaged after that.

2.2. Machine learning

We employed several well-known ML models, including the support vector classifier with a radial basis function kernel (SVC), the k-nearest neighbor model (KNN), the gaussian naive Bayes classifier (GNB) and the AdaBoost with 100 decision trees (AB) for predicting the plasticity of HEAs. A grid search with F1-score estimation was used for tuning ML models.

After that, selected ML models were trained using balanced datasets. The ML algorithms, sets of features (and their threshold values) and balancing techniques were varied to find the model with the best metrics of accuracy.

We used the next accuracy metrics: balancing accuracy, f1-score, Δ and AUC. Balancing accuracy (BA) is the macro-average of recall scores per class, or, equivalently, raw accuracy, where each sample is weighted according to the inverse prevalence of its true class (Eq.(2)).

$$BA = \frac{1}{2n}\sum\left(\frac{TP}{TP+FN}+\frac{TN}{TN+FP}\right) \tag{2}$$

where TP (True Positive) represents the frequency with which a model correctly predicts the presence of a phase, TN (True Negative) represents the frequency with which a model correctly predicts the absence of a phase, FP (False Positive) represents the frequency with which a model incorrectly predicts the presence of a phase when it is not present, and FN (False Negative) representing the frequency with which a model incorrectly predicts the absence of an actual phase.

F1-score (F1) is calculated from the precision and recall of the test, where the precision is the number of true positive results divided by the number of all samples predicted to be positive, including those not identified correctly, and the recall is the number of true positive results divided by the number of all samples that should have been identified as positive (Eq.(3)).

$$F1 = \frac{2TP}{2TP+FP+FN} \tag{3}$$

Δ is the difference between the true positive rate (TRP) and the false positive rate (FRP) (Eqs. (4)–(6)). TPR is the probability that an actual positive will test positive and FRP is the probability that a false alarm will be raised – that a positive result will be given when the true value is negative.

$$\Delta = TRP - FRP \tag{4}$$

$$TRP = \frac{TP}{TP+FN} \tag{5}$$

$$FRP = \frac{FP}{FP+TN} \tag{6}$$

The machine-learning models were checked by 6-fold cross-validation on the validation sets.

In addition to the feature cutoff threshold, a significant impact on the accuracy of the model is exerted by the classifier cutoff threshold, the value on the basis of which the continuous output values from 0 to 1 of machine learning models are converted into discrete values of binary classification (0 - non-ductile or 1 - ductile). Therefore, for all machine learning models, ROC curves (receiver operating characteristic curves) were constructed, where for each value of the feature cutoff threshold, the TPR and FPR values were calculated for different classifier cutoff threshold values. Also, as an accuracy metric, AUC (area under the curve) was calculated for each ROC curve.

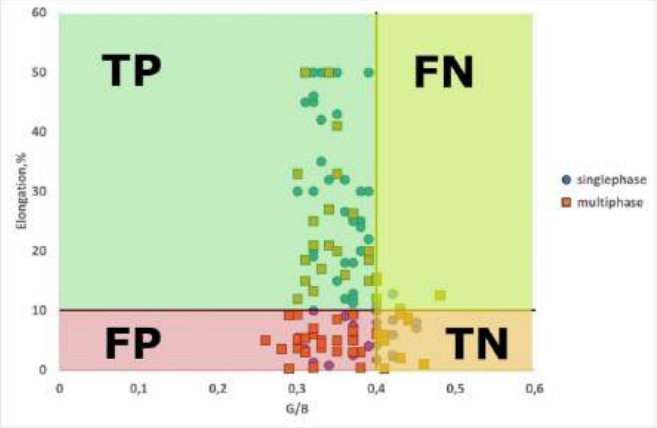

Fig. 1. Scheme for determining input data using the example of the Pettifor and Pugh model [61].

Based on the AUC values, the optimal feature cutoff value (and the set of features for training, respectively) was selected, and based on the maximum delta value for this curve, the classifier cutoff threshold value was selected for each machine learning algorithm. Next, a model was selected by comparison among various machine learning algorithms, which was subsequently used for experimental testing.

2.3. Phenomenological models for predicting plasticity

Several phenomenological models have been proposed for plasticity prediction. We used Pettifor and Pugh [61], Valence Electron Concentration (VEC) [62] and Rice and Thomson models [63] to compare with our DDML model (see Fig. 1).

Senkov and all [65] suggested that alloys with compress deformation to failure more than 30 % are considered ductile. We argue that this phenomenological threshold is not optimal. To optimize this parameter, we varied its value from the minimum to the maximum in the dataset with an increment of 0.1. For each criterion value, balanced accuracy, f1-score, TPR and FPR were calculated according to the above equations. Fig. 3 shows, using an example of the Pettifor and Pugh model, how the input data were determined for calculating accuracy metrics. As a result, the threshold of 10 % (instead of 30 %) was established as optimal for dividing into ductile and non-ductile alloys. The accuracy metrics calculated for both threshold values are presented in Table 2. For the calculations, we used a dataset on the compressive deformation of alloys with calculated parameters for these models, given in Ref. [65]. It should also be noted that the phenomenological models used for comparison were developed for single-phase alloys, and so their applicability for predicting the plasticity of multiphase alloys is a debatable issue. For that reason, accuracy metrics were calculated separately for single-phase and multiphase alloys, as well as for all systems without dividing them by phase composition.

2.4. Experiment

The model alloys were produced by vacuum arc melting, using proper mixtures of pure metals with purities of better than 99.9 wt%, in

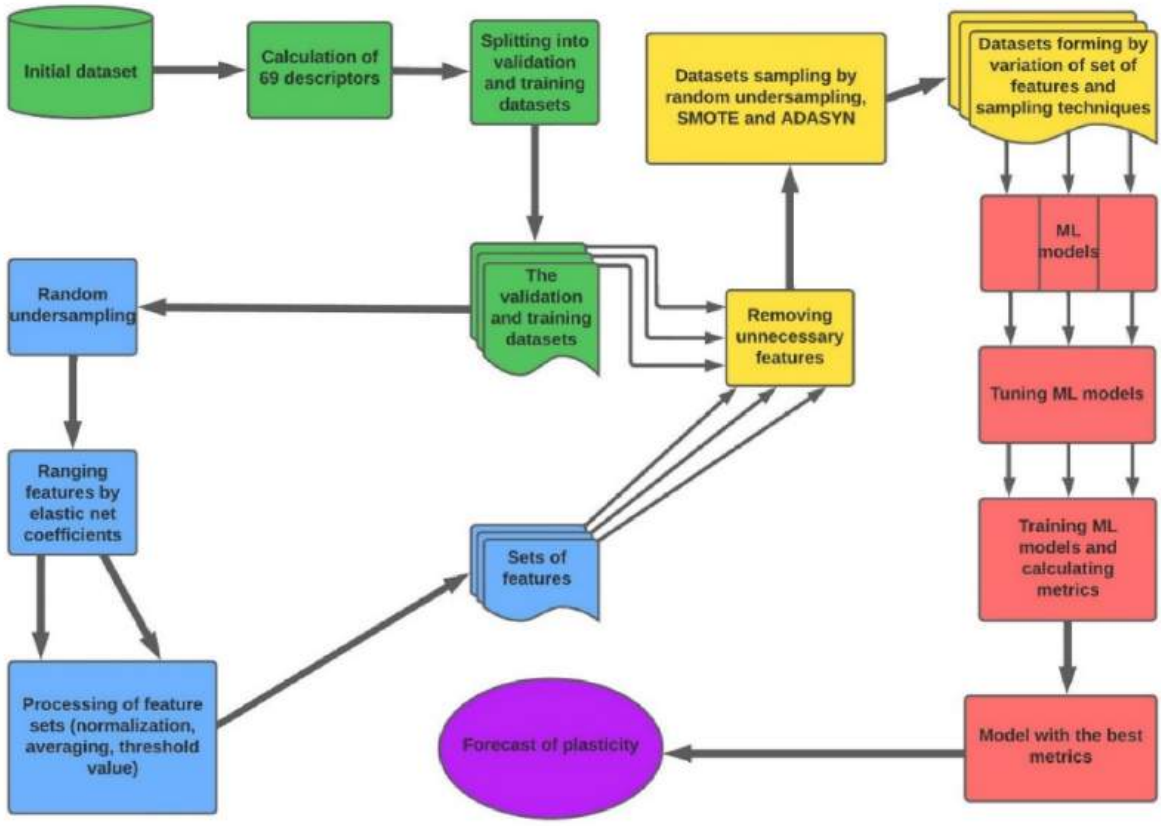

Fig. 2. General scheme for preparing the model of plasticity prediction.

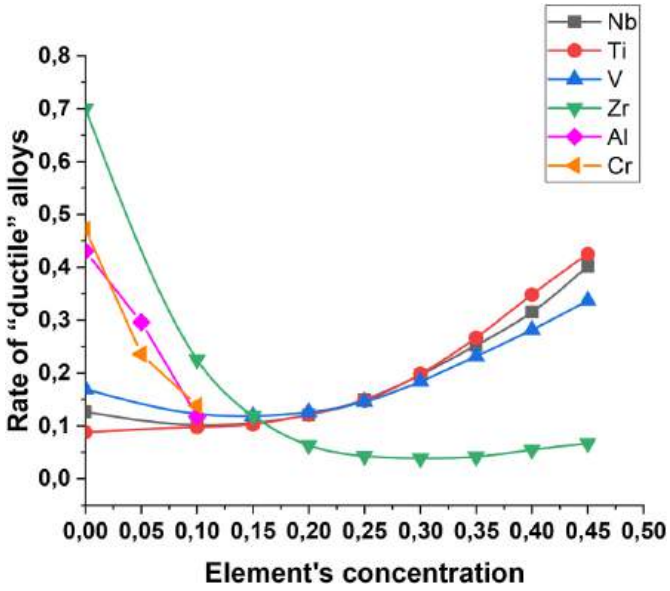

Fig. 3. Rate of ductile alloys from alloys with a fixed content of the corresponding element (other elements vary within specified limits) for the Al-Cr-Nb-Ti-V-Zr system.

Ti-gettered argon atmosphere. The nominal compositions of the model alloys are listed in Table 4, the actual compositions are listed in Supplementary materials (Fig. S3 and Table S2). The alloys were remelted five times to improve their homogeneity. Samples for compression tests and microstructure investigations were cut out using an electric discharge machine.

The phase composition was studied using X-ray diffraction (XRD) on a BRUKER D2 PHASER diffractometer with CuKα radiation. SEM investigations were carried out using either FEI Quanta 600 FEG or Nova NanoSEM microscopes; both instruments were equipped with back-scattered electron (BSE) and energy-dispersive X-ray spectroscopy (EDS) detectors. Specimens for structural investigations were finished with OP-S suspension (the abrasive particle size of 0.04 μm). The chemical composition of the alloys was measured using SEM-EDS with a scanning area of 2×2 mm^2.

Cylindric specimens measured Ø4×6 mm^3 were compressed using an Instron 300LX testing machine equipped with a radial heating furnace. The tests were carried out at 25, 600 or 800 °C with an initial strain rate of 10^{-4} s^{-1} till 50 % of height reduction (or till fracture). Temperature was measures by thermocouple attached to the side surface of the specimen; tests at 600 or 800 °C started after 10 min holding at the desired temperature.

3. results and discussion

3.1. The accuracy metrics of phenomenological models

Accuracy metrics obtained by phenomenological models with the dataset and threshold from Ref. [51] are given in Table 2 in the "Ductility alloys ≥30 %" column. As can be seen from the presented data, the models with such criteria show low accuracy for both single-phase and multi-phase alloys. The models are characterized by a strongly biased assessment towards predicting ductile alloys.

Also, as part of this work, the model was adjusted for the case when the threshold for separating "ductile" and "non-ductile" alloys is taken to 10 %. ROC-curves for all three models are given in the Supplementary materials. It has been established that the models have the best predictive force for this plasticity threshold with the following parameters:

Table 2
Accuracy metrics for phenomenological models for plasticity prediction.

Phase composition	Accuracy metrics	Ductility alloys ≥30 %			Ductility alloys≥10 %		
		VEC	G/B	GB/γ	VEC	G/B	GB/γ
Single-phase alloys	BA	0,628	0,523	0,616	0,656	0,641	0,712
	F1	0,652	0,594	0,645	0,872	0,874	0,875
	TPR	1000	1000	1000	0,962	0,981	0,925
	FPR	0,744	0,953	0,767	0,650	0,700	0,500
Multiphase alloys	BA	0,588	0,579	0,588	0,563	0,604	0,545
	F1	0,254	0,250	0,254	0,635	0,659	0,619
	TPR	1000	1000	1000	0,931	0,931	0,897
	FPR	0,825	0,842	0,825	0,806	0,722	0,806
All alloys	BA	0,608	0,551	0,602	0,609	0,622	0,629
	F1	0,453	0,422	0,450	0,754	0,766	0,747
	TPR	1000	1000	1000	0,947	0,956	0,911
	FPR	0,784	0,898	0,796	0,728	0,711	0,653

Table 3
The best values of accuracy metrics and model parameters at which they are achieved for all machine learning algorithms used.

ML algorithm	Set of feature	Balancing technique	Feature cutoff threshold	Classification cutoff threshold	AUC	Δ	BA	F1
KNN	ΔVA, ΔCPM, ΔXMB, ΔS_{mix}, ΔVEC, ΔMC, ΔNCE, ΔCE, ΔEA	SMOTE	0.4	0.5	0.972	0.824	0.711	0.758
GNB	ΔVA, ΔCPM, ΔXMB	SMOTE	0.8	0.5	0.91	0.74	0.718	0.758
AB	ΔVA, $\overline{\text{DVE}}$, ΔCPM, ΔS_{mix}, ΔNCE, XMB, $\overline{\text{WF}}$, ΔEV	ADASYN	0.3	0.5	0.982	0.982	0.72	0.786
SVC	ΔVA, $\overline{\text{DVE}}$, ΔCPM	ADASYN	0.6	0.47	0.992	0.866	0.784	0.824

Table 4
Chemical composition and predicted yield strengths for model alloys.

	Chemical composition in % at.	Predicted $\sigma_{0.2}$ at 20 °C,MPa	Predicted $\sigma_{0.2}$ at 600 °C,MPa	Plasticity at 20 °C
A1	$Al_4Cr_1Nb_{20}Ti_{35}V_5Zr_{35}$	885	800	Ductile
A2	$Al_9Cr_1Nb_{40}Ti_{25}V_{25}$	1226	800	Ductile
A3	$Al_2Cr_{13}Nb_{40}Ti_5V_{40}$	1043	717	Ductile
A4	$Al_1Cr_9Nb_{35}Ti_5V_{40}Zr_{10}$	1265	812	Ductile

VEC≤ 5.2, G/B ≤ 0.4, GB/γ ≤ 7.75. The accuracy metrics calculated at these values are given in the table in the "Ductility alloys≥10 %" column. The tune of the models has been improved accuracy metrics, in some cases quite significantly. For example, the Rice and Thomson model [63] shows good results for single-phase alloys. However, even being improved, the models have highly biased estimates; the accuracy of prediction for non-ductile alloys is much worse than for ductile alloys. For multiphase alloys or mixed phase compositions, all models, even after tuning, demonstrate low accuracy.

3.2. Selection ML model for plasticity prediction

The general scheme for developing ML model for plasticity prediction is shown in Fig. 2. The accuracy metrics were calculated for the all used machine-learning models (trained at the all datasets).

During training of models based on various machine learning algorithms, many graphs were obtained (AUC and ROC curves for all variants of training data sets). In order not to clutter the text with similar graphs, they are all presented in additional materials. Table 3 shows the models that showed the best accuracy metrics for each machine learning algorithm, as well as the parameters under which these values were achieved.

With minimal difference in accuracy metrics, SVC shows the best values of accuracy metrics. When combined with a classification cutoff threshold value of 0.47, SVC exhibits AUC = 0.992, Δ = 0.866, BA = 0.784, and F-score = 0.824. The features that were used to train each of the models presented above are shown in Table S1. The selected machine learning model shows significantly better accuracy metrics compared to the phenomenological models discussed above.

It was the SVC model with the cutoff thresholds listed above that was used further to predict plasticity.

3.3. Selection the model alloy

In order for model alloys, along with good ductility at room temperature, to show high strength, in addition to the model described above, we also used our previously developed model for predicting the yield stress at room and elevated temperatures [86]. Our model for prediction phase composition was also used for selection model alloys.

The model alloys were selected from array of Al-Cr-Nb-Ti-V-Zr alloys. The atomic concentrations of Nb, Ti, V and Zr were varied from 0 to 45 % with step 5 %, for Al and Cr the interval 0–15 % at with step 1 %. was used. According to the widely used definition of HEAs, the concentrations of elements are in the range of 5–35 %. To provide a wider coverage of the compositional space, we slightly expanded this range to 45 % for all elements except chrome and aluminum. The limitation for Al and Cr concentration is associated with our experience with alloys of this system. When the Al and Cr content is more than 15 %, most alloys have low deformation before failure, up to failure in the elastic region. Therefore, alloys with high Cr and Al content were excluded from consideration. The total number of potential alloys was ~30 000.

In the first stage, the model of plasticity prediction was applied and "non-ductile" alloys were excluded from the next calculation. To evaluate the main trends of the influence of each element on plasticity, the rate of "ductile" alloys at fixed values of the elements (Al, Cr, Nb, Ti, V or Zr) was analyzed (Fig. 3). The general feature for all elements is the parabolic-like dependence of rate of "ductile" alloys on the content of elements. But, for niobium, titanium, and vanadium, we see increasing the rate of "ductile" alloys with increasing concentration. The rate of "ductile" alloys demonstrates minimum at element concentrations of 0.1–0.15 followed by monotonous growth. The additions of small concentrations of zirconium lead to a significant decrease in ductility. Indeed, in the absence of zirconium, almost all alloys are predicted to be ductile, while with a zirconium content of 0.2 the proportion of ductile alloys is approximately 10 %. A further increase in the zirconium content does not lead to a significant change in the proportion of ductile

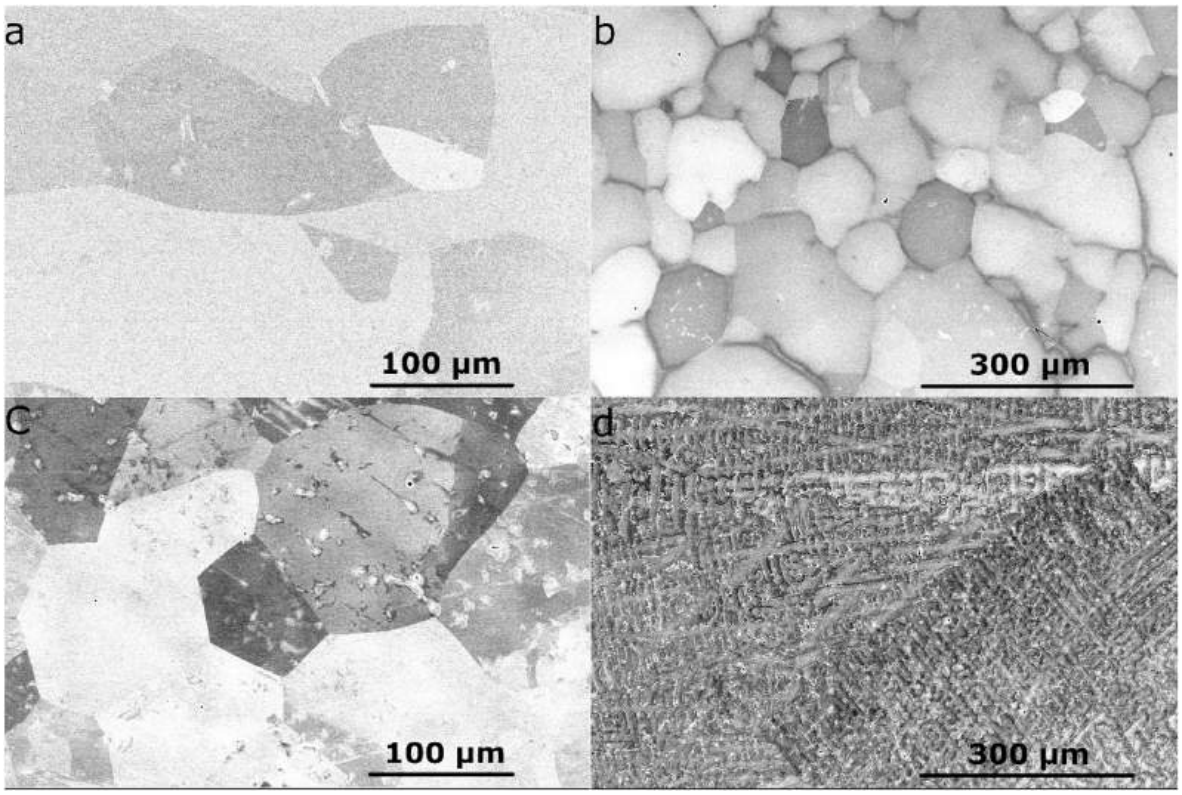

Fig. 4. SEM-BSE images of the $Al_4Cr_1Nb_{20}Ti_{35}V_5Zr_{35}$(a), $Al_9Cr_1Nb_{40}Ti_{25}V_{25}$(b), $Al_2Cr_{13}Nb_{40}Ti_5V_{40}$ (c) and $Al_1Cr_9Nb_{35}Ti_5V_{40}Zr_{10}$(d).

alloys. Concentration dependencies for aluminum and chromium reveal steps distorting their shape. But the general trend for these elements (especially the dependence on their common concentration) is similar to that for zirconium: the rate of "ductile" alloys decreases with concentration.

After plasticity prediction, the values of yield strength at 20 °C and 600 °C were calculated using the model we developed earlier [86]. Yield strengths for both temperatures were rescaled by min-max normalization. The sum of rescaled yield strengths for each alloy was used as effective strength, it was assumed that an alloy with a higher effective strength is preferable. Then, the clusters with similar compositions in phase space were selected by our model for phase composition prediction. Euclidian distance in composition space between each alloy and the center of its cluster were calculated. Based on the assumption that the precision of phase composition prediction on the cluster border's might be less than that in the central area, the alloys with small Euclidian distance in composition space were more favored. Four model alloys were selected as those with maximal values of the following quantity: $\Theta = \sigma_{YE} d_{CE}$,where σ_{YE}– effective strength, d_{CE} - Euclidian distance in composition space.

Table 4 presents data on the chemical composition of selected alloys, predicted yield strength at 20 °C and 600 °C and plasticity at room temperature for model alloys.

3.4. Microstructure and mechanical properties of model alloys

SEM images of the microstructure of the as-cast model alloys are shown in Fig. 4. The $Al_4Cr_1Nb_{20}Ti_{35}V_5Zr_{35}$ (Fig. 4a) and $Al_2Cr_{13}Nb_{40}Ti_5V_{40}$ (Fig. 4c) alloys had coarse grained (D ~100–500 μm) microstructure. According to the XRD results (Fig. S4), the alloys had bcc structure. The $Al_9Cr_1Nb_{40}Ti_{25}V_{25}$ (Fig. 4b) alloy has dual-phase structure, particles of the second phase are located at triple junctions and along the grain boundaries of the main phase. The XRD shows a single peak that does not belong to the bcc phase. This confirms the presence of the second phase, but does not allow its identification. The $Al_1Cr_9Nb_{35}Ti_5V_{40}Zr_{10}$ (Fig. 4d) shows dendritic two-phase structure composed of BCC and Laves phases (Table S2). After clarifying the chemical composition, the predicted values (yield strength and plasticity) were recalculated taking into account the actual chemical composition. The ductility forecast for all alloys has not changed. The predicted values of the yield strengths also did not show significant changes (Table 5).

The model alloys were tested at room and elevated temperatures. The engineering stress-strain curves at room temperature are shown in Fig. 5a. The values of experimental yield strength and plasticity (strain to fracture) are listed in Table 5.

As stated above, the model alloys were selected from "ductile" alloys group (fracture strain $e_F \geq 10$ % at room temperature). The three model

Table 5
Fracture strain (e_F), experimental (σ_{EY}) and predicted (σ_{PY}) yield stress for model alloy at 25, 600 and 800 °C. Predicted yield strengths were recalculated for actual chemical composition of the model alloys.

	Alloys	25 °C			600 °C			800 °C	
		σ_{EY}, MPa	σ_{PY}, MPa	e_F,%	σ_{EY}, MPa	σ_{PY}, MPa	e_F,%	σ_{EY}, MPa	e_F,%
A1	$Al_4Cr_1Nb_{20}Ti_{35}V_5Zr_{35}$	782	915	>50	550	770	>50	93	>50
A2	$Al_9Cr_1Nb_{40}Ti_{25}V_{25}$	1040	1241	>50	680	800	>50	750	>50
A3	$Al_2Cr_{13}Nb_{40}Ti_5V_{40}$	890	1073	>50	860	731	>50	780	>50
A4	$Al_1Cr_9Nb_{35}Ti_5V_{40}Zr_{10}$	1090	1289	14.7	873	825	6.9	920	>50

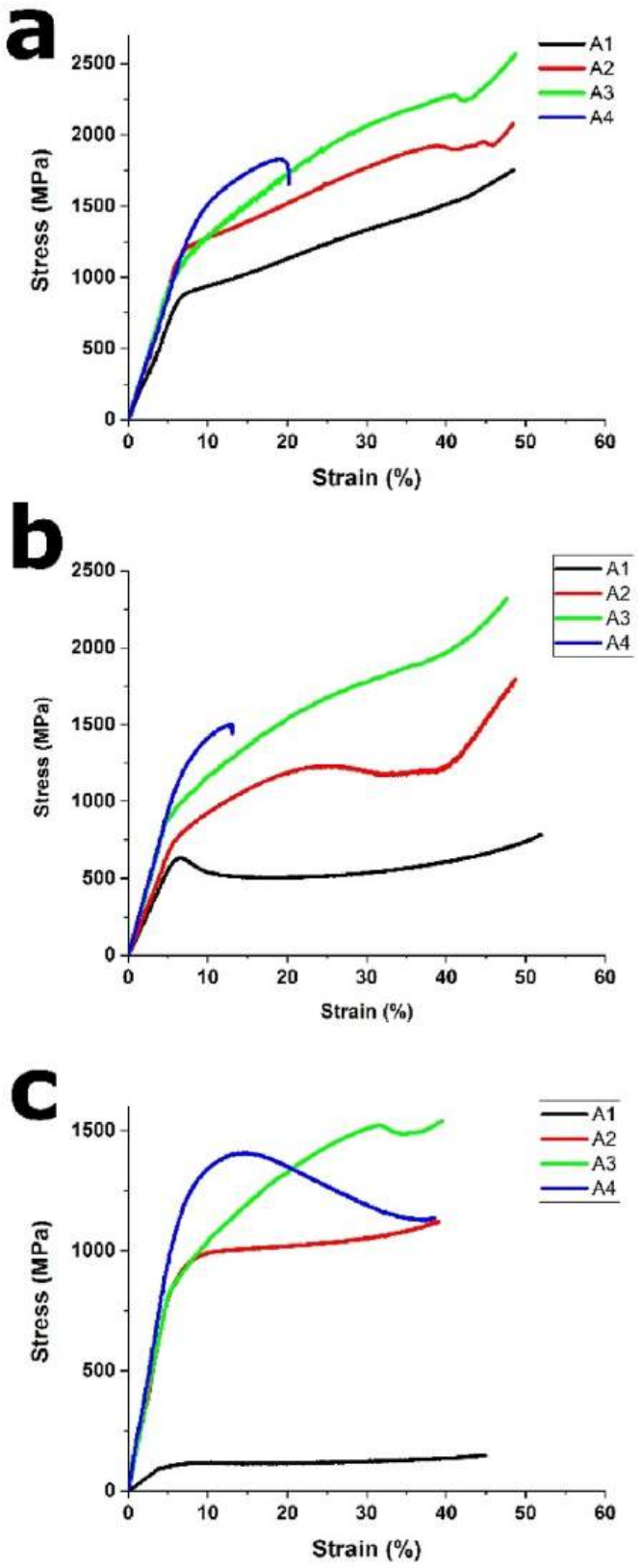

Fig. 5. Engineering stress-strain curves for model alloys at 25 °C (a), 600 °C (b) and 800 °C(c).

alloys (A1, A2, A3) not fractured until 50 % height reduction, the $Al_1Cr_9Nb_{35}Ti_5V_{40}Zr_{10}$ alloy fractured the fracture strain e_F = 14.7 %. The experimental results coincide with the prediction for all four model alloys, which confirms the high accuracy of the model on validation and test datasets. But alloy A4 showed a twofold decrease in ductility when the temperature increased to 600 °C and deformation up to 50 % without failure at 800 °C. Thus, despite the high accuracy of the prediction of ductility at room temperature, the model cannot guarantee that an alloy will be ductile over the entire temperature range.

For all fabricated model alloys, the actual yield strengths are lower than the forecasted values, average error is 18.7 %. The maximum yield strength of 1090 MPa at room temperature is demonstrated by $Al_1Cr_9Nb_{35}Ti_5V_{40}Zr_{10}$ (A4). Alloy A2 turned out to be slightly softer (σ_{EY} = 1040 MPa). The A1 and A3 alloys had yield strengths below 1000 MPa (782 MPa and 890 MPa, respectively). At 600 °C (Fig. 5b) 2 alloys show experimental yield strength that is higher than predicted value, average error is about 19 %. The strongest alloy at this temperature is A4 (σ_{EY} = 873 MPa), which is slightly higher than predicted value (σ_{PY} = 825 MPa). The A3 alloy is slightly softer than the A4. Note that the A3 alloys shows negligible softening when the testing temperature increases from 22 to 600 °C, and the experimental yield strength is higher than the predicted one at 600 °C. For the A2 alloy, an increase in testing temperature from 22 °C to 600 °C leads to a 35 % decrease in strength (σ_{EY} = 680 MPa), which is significantly less than the predicted yield strength (σ_{PY} = 800 MPa). As at room temperature, alloy A1 showed the lowest yield strength at 600 °C (σ_{EY} = 550 MPa), which is also significantly less than the predicted yield strength (σ_{PY} = 770 MPa).

With a further increase in temperature to 800 °C (Fig. 5c) for alloy A1, strong softening is observed, and the yield strength decreases to σ_{EY} = 93 MPa. For alloy A3, an increase in temperature does not lead to such a catastrophic drop in strength and respectable level of σ_{EY} = 780 MPa is maintained. For the other two alloys, an unexpected increase in the yield strength with increasing test temperature is observed. For alloy A2, the yield strength at 800 °C is σ_{EY} = 750 MPa. Alloy A4 remains the strongest among the model alloys and its yield strength is σ_{EY} = 920 MPa, which is slightly less than its yield strength at room temperature. Since this work is devoted to the prediction of the plasticity of alloys, the reasons for the anomalous temperature dependence of strength of A2 and A4 alloys are not clarified here but rather will be subject of the further studies.

4. Conclusions

1) In comparison with existing phenomenological models for predicting plasticity, our machine learning model shows significantly better accuracy. The use of machine learning approaches allows us to obtain a model that predicts the ductility of HEAs at room temperature with high accuracy. For four model alloys in agreement with the prediction, the failure strain exceeded 10 % (three alloys did not fail at deformation up to 50 %).
2) The combined use of a plasticity prediction model with previously developed models made it possible to obtain alloys with a good strength-ductility ratio both at room temperature and at elevated temperatures.
3) The fabricated $Al_1Cr_9Nb_{35}Ti_5V_{40}Zr_{10}$ alloy reveals the best combination of strength and ductility both at room temperature (σ_{EY} = 1090 MPa, e_F = 14.7 %) and at 800 °C (σ_{EY} = 920 MPa, e_F >50 %).

CRediT authorship contribution statement

Denis Klimenko: Writing – original draft, Visualization, Validation, Software, Investigation. **Nikita Stepanov:** Writing – review & editing, Resources, Formal analysis, Conceptualization. **Roman Ryltsev:** Writing – review & editing, Validation, Formal analysis. **Nikita Yurchenko:** Resources, Data curation. **Sergey Zherebtsov:** Writing – review & editing, Supervision, Resources, Project administration,

Conceptualization.

Declaration of competing interest

The authors declare that they have no known competing financial interests or personal relationships that could have appeared to influence the work reported in this paper.

Data availability

Data will be made available on request.

Acknowledgments

The authors gratefully acknowledge the financial support from the Russian Science Foundation Grant no. 19-79-30066 (https://rscf.ru/en/project/19-79-30066/). The work was carried out using the equipment of the Joint Research Center of Belgorod State National Research University « Technology and Materials». A part of this research (XRD analysis) was partially funded by the Ministry of Science and Higher Education of the Russian Federation as part of the World-Class Research Centre program: Advanced Digital Technologies (Contract no. № 075–15–2022–312 dated April 20, 2022).

Appendix A. Supplementary data

Supplementary data to this article can be found online at https://doi.org/10.1016/j.intermet.2024.108469.

References

[1] M.C. Gao, P.K. Liaw, J.W. Yeh, Y. Zhang, High-entropy alloys: Fundamentals and applications (2016), https://doi.org/10.1007/978-3-319-27013-5.
[2] B. Cantor, I.T.H. Chang, P. Knight, A.J.B. Vincent, Microstructural development in equiatomic multicomponent alloys, Mater. Sci. Eng. 375–377 (2004) 213–218, https://doi.org/10.1016/j.msea.2003.10.257.
[3] E.P. George, D. Raabe, R.O. Ritchie, High-entropy alloys, Nat. Rev. Mater. 4 (2019) 515–534, https://doi.org/10.1038/s41578-019-0121-4.
[4] F. Otto, Y. Yang, H. Bei, E.P. George, Relative effects of enthalpy and entropy on the phase stability of equiatomic high-entropy alloys, Acta Mater. 61 (2013) 2628–2638, https://doi.org/10.1016/j.actamat.2013.01.042.
[5] D. Ma, B. Grabowski, F. Körmann, J. Neugebauer, D. Raabe, Ab initio thermodynamics of the CoCrFeMnNi high entropy alloy: importance of entropy contributions beyond the configurational one, Acta Mater. 100 (2015) 90–97, https://doi.org/10.1016/j.actamat.2015.08.050.
[6] B. Cantor, Multicomponent high-entropy Cantor alloys, Prog. Mater. Sci. 120 (2021) 100754, https://doi.org/10.1016/j.pmatsci.2020.100754.
[7] Y. Zhang, T.T. Zuo, Z. Tang, M.C. Gao, K.A. Dahmen, P.K. Liaw, Z.P. Lu, Microstructures and properties of high-entropy alloys, Prog. Mater. Sci. 61 (2014) 1–93, https://doi.org/10.1016/j.pmatsci.2013.10.001.
[8] M.H. Tsai, J.W. Yeh, High-entropy alloys: a critical review, Mater Res Lett 2 (2014) 107–123, https://doi.org/10.1080/21663831.2014.912690.
[9] D.B. Miracle, O.N. Senkov, A critical review of high entropy alloys and related concepts, Acta Mater. 122 (2017) 448–511, https://doi.org/10.1016/j.actamat.2016.08.081.
[10] Y. Ikeda, B. Grabowski, F. Körmann, Ab initio phase stabilities and mechanical properties of multicomponent alloys: a comprehensive review for high entropy alloys and compositionally complex alloys, Mater. Char. 147 (2019) 464–511, https://doi.org/10.1016/j.matchar.2018.06.019.
[11] E.P. George, W.A. Curtin, C.C. Tasan, High entropy alloys: a focused review of mechanical properties and deformation mechanisms, Acta Mater. 188 (2020) 435–474, https://doi.org/10.1016/j.actamat.2019.12.015.
[12] W. Steurer, Single-phase high-entropy alloys – a critical update, Mater. Char. 162 (2020) 110179, https://doi.org/10.1016/j.matchar.2020.110179.
[13] M.H. Chuang, M.H. Tsai, W.R. Wang, S.J. Lin, J.W. Yeh, Microstructure and wear behavior of AlxCo 1.5CrFeNi1.5Tiy high-entropy alloys, Acta Mater. 59 (2011) 6308–6317, https://doi.org/10.1016/j.actamat.2011.06.041.
[14] B. Gorr, M. Azim, H.J. Christ, T. Mueller, D. Schliephake, M. Heilmaier, Phase equilibria, microstructure, and high temperature oxidation resistance of novel refractory high-entropy alloys, J. Alloys Compd. 624 (2015) 270–278, https://doi.org/10.1016/j.jallcom.2014.11.012.
[15] Y. Shi, B. Yang, P.K. Liaw, Corrosion-resistant high-entropy alloys: a review, Metals 7 (2017) 1–18, https://doi.org/10.3390/met7020043.
[16] N.Y. Yurchenko, E.S. Panina, S.V. Zherebtsov, M.A. Tikhonovsky, G.A. Salishchev, N.D. Stepanov, Microstructure evolution of a novel low-density Ti–Cr–Nb–V refractory high entropy alloy during cold rolling and subsequent annealing, Mater. Char. 158 (2019), https://doi.org/10.1016/j.matchar.2019.109980.
[17] N. Yurchenko, E. Panina, M. Tikhonovsky, G. Salishchev, S. Zherebtsov, N. Stepanov, Structure and mechanical properties of an in situ refractory Al20Cr10Nb15Ti20V25Zr10 high entropy alloy composite, Mater. Lett. 264 (2020), https://doi.org/10.1016/j.matlet.2020.127372.
[18] O.N. Senkov, G.B. Wilks, J.M. Scott, D.B. Miracle, Mechanical properties of Nb25Mo25Ta 25W25 and V20Nb20Mo 20Ta20W20 refractory high entropy alloys, Intermetallics 19 (2011) 698–706, https://doi.org/10.1016/j.intermet.2011.01.004.
[19] O.N. Senkov, G.B. Wilks, D.B. Miracle, C.P. Chuang, P.K. Liaw, Refractory high-entropy alloys, Intermetallics 18 (2010) 1758–1765, https://doi.org/10.1016/j.intermet.2010.05.014.
[20] O.N. Senkov, J.M. Scott, S.V. Senkova, F. Meisenkothen, D.B. Miracle, C. F. Woodward, Microstructure and elevated temperature properties of a refractory TaNbHfZrTi alloy, J. Mater. Sci. 47 (2012) 4062–4074, https://doi.org/10.1007/s10853-012-6260-2.
[21] O.N. Senkov, C.F. Woodward, Microstructure and properties of a refractory NbCrMo0.5Ta0.5TiZr alloy, Mater. Sci. Eng., A 529 (2011) 311–320, https://doi.org/10.1016/j.msea.2011.09.033.
[22] O.N. Senkov, D. Isheim, D.N. Seidman, A.L. Pilchak, Development of a refractory high entropy superalloy, Entropy 18 (2016) 1–13, https://doi.org/10.3390/e18030102.
[23] O.N. Senkov, S.V. Senkova, D.B. Miracle, C. Woodward, Mechanical properties of low-density, refractory multi-principal element alloys of the Cr-Nb-Ti-V-Zr system, Mater. Sci. Eng., A 565 (2013) 51–62, https://doi.org/10.1016/j.msea.2012.12.018.
[24] N.Y. Yurchenko, E.S. Panina, G. Salishchev, N.D. Stepanov, Design and characterization of Al-Cr-Nb-Ti-V-Zr high-entropy alloys for high-temperature applications, Phys. Mesomech. 24 (2021) 642–652, https://doi.org/10.1134/S1029959921060023.
[25] D. Farkas, A. Caro, Model interatomic potentials and lattice strain in a high-entropy alloy, J. Mater. Res. 33 (2018) 3218–3225, https://doi.org/10.1557/jmr.2018.245.
[26] W.M. Choi, J.S. Kim, W.S. Ko, D.G. Kim, Y.H. Jo, S.S. Sohn, S. Lee, B.J. Lee, Computational design of V-CoCrFeMnNi high-entropy alloys: an atomistic simulation study, Calphad 74 (2021) 102317, https://doi.org/10.1016/j.calphad.2021.102317.
[27] M. Widom, Modeling the structure and thermodynamics of high-entropy alloys, J. Mater. Res. 33 (2018) 2881–2898, https://doi.org/10.1557/jmr.2018.222.
[28] A. Daramola, G. Bonny, G. Adjanor, C. Domain, G. Monnet, A. Fraczkiewicz, Development of a plasticity-oriented interatomic potential for CrFeMnNi high entropy alloys, Comput. Mater. Sci. 203 (2022) 111165, https://doi.org/10.1016/j.commatsci.2021.111165.
[29] J. Ding, Q. Yu, M. Asta, R.O. Ritchie, Tunable stacking fault energies by tailoring local chemical order in CrCoNi medium-entropy alloys, Proc. Natl. Acad. Sci. U. S. A. 115 (2018) 8919–8924, https://doi.org/10.1073/pnas.1808660115.
[30] R. Zhang, S. Zhao, J. Ding, Y. Chong, T. Jia, C. Ophus, M. Asta, R.O. Ritchie, A. M. Minor, Short-range order and its impact on the CrCoNi medium-entropy alloy, Nature 581 (2020) 283–287, https://doi.org/10.1038/s41586-020-2275-z.
[31] X. Chen, Q. Wang, Z. Cheng, M. Zhu, H. Zhou, P. Jiang, L. Zhou, Q. Xue, F. Yuan, J. Zhu, X. Wu, E. Ma, Direct observation of chemical short-range order in a medium-entropy alloy, Nature 592 (2021) 712–716, https://doi.org/10.1038/s41586-021-03428-z.
[32] N. Yurchenko, E. Panina, A. Tojibaev, V. Novikov, G. Salishchev, S. Zherebtsov, N. Stepanov, Effect of B2 ordering on the tensile mechanical properties of refractory AlxNb40Ti40V20−x medium-entropy alloys, J. Alloys Compd. 937 (2023) 168465, https://doi.org/10.1016/j.jallcom.2022.168465.
[33] T.M. Smith, M.S. Hooshmand, B.D. Esser, F. Otto, D.W. Mccomb, E.P. George, M. Ghazisaeidi, M.J. Mills, Atomic-scale characterization and modeling of 60°dislocations in a high-entropy alloy, Acta Mater. 110 (2016) 352–363, https://doi.org/10.1016/j.actamat.2016.03.045.
[34] X. Liu, Z. Pei, M. Eisenbach, Dislocation core structures and Peierls stresses of the high-entropy alloy NiCoFeCrMn and its subsystems, Mater. Des. 180 (2019) 107955, https://doi.org/10.1016/j.matdes.2019.107955.
[35] S.N. Khan, M. Eisenbach, Density-functional Monte-Carlo simulation of CuZn order-disorder transition, Phys. Rev. B 93 (2016) 1–5, https://doi.org/10.1103/PhysRevB.93.024203.
[36] Y. Gao, K. Chong, C. Liu, Y. Cao, T. Xue, F. Guo, Y. Zou, The improvement of room temperature plasticity of refractory high entropy alloy based on different first principles calculation models and experiment verification, J. Mater. Res. Technol. 26 (2023) 3917–3932, https://doi.org/10.1016/j.jmrt.2023.08.149.
[37] I. Toda-Caraballo, A general formulation for solid solution hardening effect in multicomponent alloys, Scripta Mater. 127 (2017) 113–117, https://doi.org/10.1016/j.scriptamat.2016.09.009.
[38] I. Toda-Caraballo, P.E.J. Rivera-Díaz-Del-Castillo, Modelling solid solution hardening in high entropy alloys, Acta Mater. 85 (2015) 14–23, https://doi.org/10.1016/j.actamat.2014.11.014.
[39] Z. Wang, Q. Fang, J. Li, B. Liu, Y. Liu, Effect of lattice distortion on solid solution strengthening of BCC high-entropy alloys, J. Mater. Sci. Technol. 34 (2018) 349–354, https://doi.org/10.1016/j.jmst.2017.07.013.
[40] F.G. Coury, M. Kaufman, A.J. Clarke, Solid-solution strengthening in refractory high entropy alloys, Acta Mater. 175 (2019) 66–81, https://doi.org/10.1016/j.actamat.2019.06.006.
[41] D. Peirce, R.J. Asaro, A. Needleman, An analysis of nonuniform and localized deformation in ductile single crystals, Acta Metall. 30 (1982) 1087–1119, https://doi.org/10.1016/0001-6160(82)90005-0.

[42] M. Grujicic, S. Batchu, Crystal plasticity analysis of earing in deep-drawn OFHC copper cups, J. Mater. Sci. 37 (2002) 753–764, https://doi.org/10.1023/A:1013839914584.
[43] A. Ma, F. Roters, D. Raabe, A dislocation density based constitutive model for crystal plasticity FEM including geometrically necessary dislocations, Acta Mater. 54 (2006) 2169–2179, https://doi.org/10.1016/j.actamat.2006.01.005.
[44] E.B. Marin, D.L. McDowell, A semi-implicit integration scheme for rate-dependent and rate-independent plasticity, Comput. Struct. 63 (1997) 579–600, https://doi.org/10.1016/S0045-7949(97)89625-3.
[45] H.W. Li, H. Yang, Z.C. Sun, A robust integration algorithm for implementing rate dependent crystal plasticity into explicit finite element method, Int. J. Plast. 24 (2008) 267–288, https://doi.org/10.1016/j.ijplas.2007.03.014.
[46] R.D. McGinty, D.L. McDowell, A semi-implicit integration scheme for rate independent finite crystal plasticity, Int. J. Plast. 22 (2006) 996–1025, https://doi.org/10.1016/j.ijplas.2005.06.002.
[47] S. Guo, Phase selection rules for cast high entropy alloys: an overview, Mater. Sci. Technol. 31 (2015) 1223–1230, https://doi.org/10.1179/1743284715Y.0000000018.
[48] X. Yang, Y. Zhang, Prediction of high-entropy stabilized solid-solution in multi-component alloys, Mater. Chem. Phys. 132 (2012) 233–238, https://doi.org/10.1016/j.matchemphys.2011.11.021.
[49] S. Guo, Q. Hu, C. Ng, C.T. Liu, More than entropy in high-entropy alloys: forming solid solutions or amorphous phase, Intermetallics 41 (2013) 96–103, https://doi.org/10.1016/j.intermet.2013.05.002.
[50] Y.F. Ye, Q. Wang, J. Lu, C.T. Liu, Y. Yang, Design of high entropy alloys: a single-parameter thermodynamic rule, Scripta Mater. 104 (2015) 53–55, https://doi.org/10.1016/j.scriptamat.2015.03.023.
[51] A.K. Singh, N. Kumar, A. Dwivedi, A. Subramaniam, A geometrical parameter for the formation of disordered solid solutions in multi-component alloys, Intermetallics 53 (2014) 112–119, https://doi.org/10.1016/j.intermet.2014.04.019.
[52] Z. Wang, Y. Huang, Y. Yang, J. Wang, C.T. Liu, Atomic-size effect and solid solubility of multicomponent alloys, Scripta Mater. 94 (2015) 28–31, https://doi.org/10.1016/j.scriptamat.2014.09.010.
[53] M.C. Troparevsky, J.R. Morris, P.R.C. Kent, A.R. Lupini, G.M. Stocks, Criteria for predicting the formation of single-phase high-entropy alloys, Phys. Rev. X 5 (2015) 1–6, https://doi.org/10.1103/PhysRevX.5.011041.
[54] D.J.M. King, S.C. Middleburgh, A.G. McGregor, M.B. Cortie, Predicting the formation and stability of single phase high-entropy alloys, Acta Mater. 104 (2016) 172–179, https://doi.org/10.1016/j.actamat.2015.11.040.
[55] O.N. Senkov, D.B. Miracle, A new thermodynamic parameter to predict formation of solid solution or intermetallic phases in high entropy alloys, J. Alloys Compd. 658 (2016) 603–607, https://doi.org/10.1016/j.jallcom.2015.10.279.
[56] M.G. Poletti, L. Battezzati, Electronic and thermodynamic criteria for the occurrence of high entropy alloys in metallic systems, Acta Mater. 75 (2014) 297–306, https://doi.org/10.1016/j.actamat.2014.04.033.
[57] S. Guo, C. Ng, J. Lu, C.T. Liu, Effect of valence electron concentration on stability of fcc or bcc phase in high entropy alloys, J. Appl. Phys. 109 (2011), https://doi.org/10.1063/1.3587228.
[58] Y. Zhang, Z.P. Lu, S.G. Ma, P.K. Liaw, Z. Tang, Y.Q. Cheng, M.C. Gao, Guidelines in predicting phase formation of high-entropy alloys, MRS Commun 4 (2014) 57–62, https://doi.org/10.1557/mrc.2014.11.
[59] O.N. Senkov, D.B. Miracle, Generalization of intrinsic ductile-to-brittle criteria by Pugh and Pettifor for materials with a cubic crystal structure, Sci. Rep. 11 (2021) 10–13, https://doi.org/10.1038/s41598-021-83953-z.
[60] S. Sheikh, S. Shafeie, Q. Hu, J. Ahlström, C. Persson, J. Veselý, J. Zýka, U. Klement, S. Guo, Alloy design for intrinsically ductile refractory high-entropy alloys, J. Appl. Phys. 120 (2016), https://doi.org/10.1063/1.4966659.
[61] J.R. Rice, R. Thomson, Ductile versus brittle behaviour of crystals, Phil. Mag. 29 (1974) 73–97, https://doi.org/10.1080/14786437408213555.
[62] J.H. Li, M.H. Tsai, Theories for predicting simple solid solution high-entropy alloys: classification, accuracy, and important factors impacting accuracy, Scripta Mater. 188 (2020) 80–87, https://doi.org/10.1016/j.scriptamat.2020.06.064.
[63] O.N. Senkov, D.B. Miracle, S.I. Rao, Correlations to improve room temperature ductility of refractory complex concentrated alloys, Mater. Sci. Eng., A 820 (2021) 141512, https://doi.org/10.1016/j.msea.2021.141512.
[64] D.B. Miracle, O.N. Senkov, A critical review of high entropy alloys and related concepts, Acta Mater. 122 (2017) 448–511, https://doi.org/10.1016/j.actamat.2016.08.081.
[65] S. Sheikh, S. Shafeie, Q. Hu, J. Ahlström, C. Persson, J. Veselý, J. Zýka, U. Klement, S. Guo, Alloy design for intrinsically ductile refractory high-entropy alloys, J. Appl. Phys. 120 (2016), https://doi.org/10.1063/1.4966659.
[66] Y. Lecun, Y. Bengio, G. Hinton, Deep learning, Nature 521 (2015) 436–444, https://doi.org/10.1038/nature14539.
[67] A. Ferrari, B. Dutta, K. Gubaev, Y. Ikeda, P. Srinivasan, B. Grabowski, F. Körmann, Frontiers in atomistic simulations of high entropy alloys, J. Appl. Phys. 128 (2020), https://doi.org/10.1063/5.0025310.
[68] V.L. Deringer, N. Bernstein, G. Csányi, C. Ben Mahmoud, M. Ceriotti, M. Wilson, D. A. Drabold, S.R. Elliott, Origins of structural and electronic transitions in disordered silicon, Nature 589 (2021) 59–64, https://doi.org/10.1038/s41586-020-03072-z.
[69] T.J. Gao, D. Zhao, T.W. Zhang, T. Jin, S.G. Ma, Z.H. Wang, Strain-rate-sensitive mechanical response, twinning, and texture features of NiCoCrFe high-entropy alloy: experiments, multi-level crystal plasticity and artificial neural networks modeling, J. Alloys Compd. 845 (2020), https://doi.org/10.1016/j.jallcom.2020.155911.
[70] T. Mueller, A. Kusne, R. Ramprasad, Science : recent progress, Rev. Comput. Chem. 29 (2016) 186–273.
[71] X. Liu, J. Zhang, Z. Pei, Machine learning for high-entropy alloys: progress, challenges and opportunities, Prog. Mater. Sci. 131 (2023) 101018, https://doi.org/10.1016/j.pmatsci.2022.101018.
[72] S. Risal, W. Zhu, P. Guillen, L. Sun, Improving phase prediction accuracy for high entropy alloys with Machine learning, Comput. Mater. Sci. 192 (2021) 110389, https://doi.org/10.1016/j.commatsci.2021.110389.
[73] Z. Zhou, Y. Zhou, Q. He, Z. Ding, F. Li, Y. Yang, Machine learning guided appraisal and exploration of phase design for high entropy alloys, npj Comput. Mater. 5 (2019) 1–9, https://doi.org/10.1038/s41524-019-0265-1.
[74] N. Islam, W. Huang, H.L. Zhuang, Machine learning for phase selection in multi-principal element alloys, Comput. Mater. Sci. 150 (2018) 230–235, https://doi.org/10.1016/j.commatsci.2018.04.003.
[75] W. Huang, P. Martin, H.L. Zhuang, Machine-learning phase prediction of high-entropy alloys, Acta Mater. 169 (2019) 225–236, https://doi.org/10.1016/j.actamat.2019.03.012.
[76] Y. Zhang, C. Wen, C. Wang, S. Antonov, D. Xue, Y. Bai, Y. Su, Phase prediction in high entropy alloys with a rational selection of materials descriptors and machine learning models, Acta Mater. 185 (2020) 528–539, https://doi.org/10.1016/j.actamat.2019.11.067.
[77] U.K. Jaiswal, Y. Vamsi Krishna, M.R. Rahul, G. Phanikumar, Machine learning-enabled identification of new medium to high entropy alloys with solid solution phases, Comput. Mater. Sci. 197 (2021) 110623, https://doi.org/10.1016/j.commatsci.2021.110623.
[78] R. Machaka, Machine learning-based prediction of phases in high-entropy alloys, Comput. Mater. Sci. 188 (2021) 110244, https://doi.org/10.1016/j.commatsci.2020.110244.
[79] B. Chanda, P.P. Jana, J. Das, A tool to predict the evolution of phase and Young's modulus in high entropy alloys using artificial neural network, Comput. Mater. Sci. 197 (2021) 110619, https://doi.org/10.1016/j.commatsci.2021.110619.
[80] S. Dixit, V. Singhal, A. Agarwal, A.K. Prasada Rao, Multi-label phase-prediction in high-entropy-alloys using Artificial-Neural-Network, Mater. Lett. 268 (2020) 127606, https://doi.org/10.1016/j.matlet.2020.127606.
[81] D. Klimenko, N. Stepanov, R. Ryltsev, S. Zherebtsov, Phase prediction in high-entropy alloys with multi-label artificial neural network, Intermetallics 151 (2022) 107722, https://doi.org/10.1016/j.intermet.2022.107722.
[82] J. Qi, D.I. Hoyos, S.J. Poon, Machine learning-based classification, interpretation, and prediction of high-entropy-alloy intermetallic phases, High Entropy Alloys & Materials 1 (2023) 312–326, https://doi.org/10.1007/s44210-023-00017-9.
[83] C. Wen, Y. Zhang, C. Wang, D. Xue, Y. Bai, S. Antonov, L. Dai, T. Lookman, Y. Su, Machine learning assisted design of high entropy alloys with desired property, Acta Mater. 170 (2019) 109–117, https://doi.org/10.1016/j.actamat.2019.03.010.
[84] R. Ramprasad, R. Batra, G. Pilania, A. Mannodi-Kanakkithodi, C. Kim, Machine learning in materials informatics: recent applications and prospects, npj Comput. Mater. 3 (2017), https://doi.org/10.1038/s41524-017-0056-5.
[85] D.N. Klimenko, N.Y. Yurchenko, N.D. Stepanov, S.V. Zherebtsov, Prediction of strength characteristics of high-entropy alloys Al-Cr-Nb-Ti-V-Zr systems, Mater. Today Proc. 38 (2021) 1535–1540, https://doi.org/10.1016/j.matpr.2020.08.145.
[86] D. Klimenko, N. Stepanov, J. Li, Q. Fang, S. Zherebtsov, Machine learning-based strength prediction for refractory high-entropy alloys of the Al-Cr-Nb-Ti-V-Zr system, Materials 14 (2021), https://doi.org/10.3390/ma14237213.
[87] Z. Pei, J. Yin, Machine learning as a contributor to physics: understanding Mg alloys, Mater. Des. 172 (2019) 107759, https://doi.org/10.1016/j.matdes.2019.107759.
[88] C. Wen, H. Shen, Y. Tian, G. Lou, N. Wang, Y. Su, Accelerated discovery of refractory high-entropy alloys for strength-ductility co-optimization: an exploration in NbTaZrHfMo system by machine learning, Scripta Mater. 252 (2024) 116240, https://doi.org/10.1016/j.scriptamat.2024.116240.
[89] L.M. Ghiringhelli, J. Vybiral, S.V. Levchenko, C. Draxl, M. Scheffler, Big data of materials science: critical role of the descriptor, Phys. Rev. Lett. 114 (2015), https://doi.org/10.1103/PhysRevLett.114.105503.
[90] U. Bhandari, M.R. Rafi, C. Zhang, S. Yang, Yield strength prediction of high-entropy alloys using machine learning, Mater. Today Commun. 26 (2021) 101871, https://doi.org/10.1016/j.mtcomm.2020.101871.